IEEE Access
Multidisciplinary ⋮ Rapid Review ⋮ Open Access Journal

Received July 28, 2020, accepted August 10, 2020, date of publication August 17, 2020, date of current version August 28, 2020.

Digital Object Identifier 10.1109/ACCESS.2020.3017440

Modeling, Localization, and Segmentation of the Foveal Avascular Zone on Retinal OCT-Angiography Images

ENRIQUE J. CARMONA[1], MACARENA DÍAZ[2,3], JORGE NOVO[2,3], AND MARCOS ORTEGA[2,3]

[1]Department of Artificial Intelligence, ETS Ingeniería Informática, Universidad Nacional de Educación a Distancia (UNED), 28040 Madrid, Spain
[2]Department of Computer Science and Information Technologies, University of A Coruña, 15008 A Coruña, Spain
[3]CITIC-Research Center of Information and Communication Technologies, University of A Coruña, 15008 A Coruña, Spain

Corresponding author: Enrique J. Carmona (ecarmona@dia.uned.es)

This work was supported by the Ministerio de Ciencia, Innovación y Universidades, Government of Spain, through the RTI2018-095894-B-I00 research project.

ABSTRACT The Foveal Avascular Zone (FAZ) is a capillary-free area that is placed inside the macula and its morphology and size represent important biomarkers to detect different ocular pathologies such as diabetic retinopathy, impaired vision or retinal vein occlusion. Therefore, an adequate and precise segmentation of the FAZ presents a high clinical interest. About to this, Angiography by Optical Coherence Tomography (OCT-A) is a non-invasive imaging technique that allows the expert to visualize the vascular and avascular foveal zone. In this work, we present a robust methodology composed of three stages to model, localize, and segment the FAZ in OCT-A images. The first stage is addressed to generate two FAZ normality models: superficial and deep plexus. The second one uses the FAZ model as a template to localize the FAZ center. Finally, in the third stage, an adaptive binarization is proposed to segment the entire FAZ region. A method based on this methodology was implemented and validated in two OCT-A image subsets, presenting the second subset more challenging pathological conditions than the first. We obtained localization success rates of 100% and 96% in the first and second subsets, respectively, considering a success if the obtained FAZ center is inside the FAZ area segmented by an expert clinician. Complementary, the Dice score and other indexes (Jaccard index and Hausdorff distance) are used to measure the segmentation quality, obtaining competitive average values in the first subset: 0.84 ± 0.01 (expert 1) and 0.85 ± 0.01 (expert 2). The average Dice score obtained in the second subset was also acceptable (0.70 ± 0.17), even though the segmentation process is more complex in this case.

INDEX TERMS Foveal avascular zone, OCT-angiography, modeling, localization, segmentation.

I. INTRODUCTION

Optical Coherence Tomography Angiography (OCT-A) [1] represents a new image modality that is commonly used in the ophthalmic field and allows the expert to visualize non-invasively the vascularization at different levels of the retinal layers. The OCT-A image acquisition process is complex. It can be divided into several steps, as we can graphically see in Fig. 1. Specifically, in step 1, it is necessary to extract several OCT images in the region of interest by forming a cube of OCT images. This process is repeated several times, being obtained different OCT cubes at different consecutive moments in time. This is necessary to compare the respective sections and generate OCT images with the vascular differences between subsequent moments in time. Note that the tissue remains fixed while the blood flow varies between respective sections as time advances. Once the differences are calculated, we obtain a new OCT cube where the blood vessels are highlighted in each section (step 2). Finally, by selecting the desired layer (superficial or deep), which is specified by the configuration of the OCT-A capture device, the cross-section of the cube is made in the region of interest, being the final OCT-A image obtained (step 3). Usually, OCT-A images are inspected by the expert clinicians in two different depth configurations: superficial and deep plexus; both of them representing the more relevant regions

The associate editor coordinating the review of this manuscript and approving it for publication was Anandakumar Haldorai.

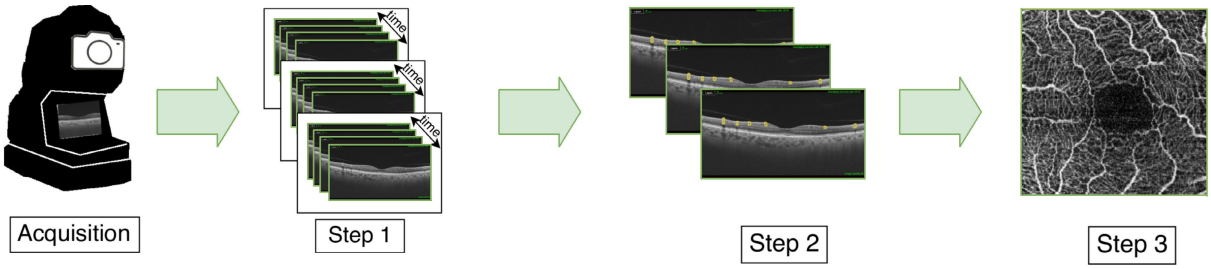

FIGURE 1. Representative steps of the OCT-A image acquisition.

of interest. The superficial plexus allows us the visualization and analysis of the main retinal vessels, while the deep plexus contains the deepest vessel information. Additionally, once selected the depth to analyze, there are two typical levels of zoom that are commonly used in the clinical field (3×3 mm^2 or 6×6 mm^2), allowing us to see a region of smaller area and higher resolution or a region of a larger area and lower resolution, respectively.

Retinal microcirculation represents valuable information in the diagnosis and monitoring process of different systemic and eye diseases that directly affect the blood flow, as could be the retinal vein occlusion or diabetes, among others. In this sense, the non-invasive imaging feature, which is associated with OCT-A, implies a clear advantage over previous imaging modalities. Furthermore, with OCT-A, it is possible to analyze small regions, providing the option of monitoring the more insignificant changes that can be relevant in the disease identification process. In particular, one of these regions is the foveal avascular zone (FAZ), whose morphology and size represent relevant clinical biomarkers that have been recurrently analyzed in different ophthalmic image modalities [2]. The value of the parameters that measure these two properties change with different diseases or phases of the same pathology. In this sense, OCT-A allows us the visualization of the FAZ region with a high level of quality, given that the images are typically captured centered in this region. In Fig. 2, we can see some representative examples of variable FAZ shapes and sizes, clearly intuiting the usefulness of the study of this region in the clinical diagnostic and monitoring process: the FAZ in healthy subjects (Fig. 2.a) is characterized by a regular circular contour and a small size; on the contrary, the FAZ contour in pathological cases (Fig. 2.b and 2.c) is more irregular and presents larger sizes.

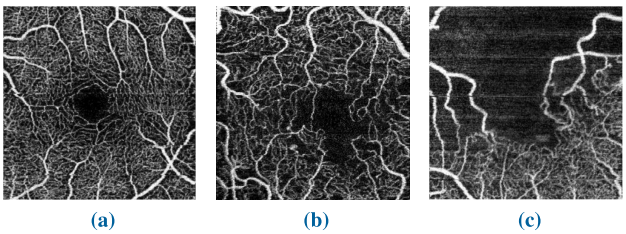

FIGURE 2. Representative examples of the variation of the FAZ area and contour in different OCT-A images and scenarios: (a) without pathology, (b) diabetic retinopathy, and (c) retinal vein occlusion.

There is a high number of clinical studies that analyze the FAZ in OCT-A images. The FAZ is related to the visual acuity of the patient in different diseases, as could be diabetic retinopathy (DR) and retinal vein occlusion [3]–[5], among others [6]. In the same line, there are clinical studies that demonstrate that the FAZ area varies with healthy and pathological subjects [7], [8], as well as with different degrees of the same disease [9]. Additionally, it has also been discovered that the size of the FAZ region changes with some risk habits, as occurs, for example, with tobacco consumption [10]. In any case, not only the FAZ size is relevant, it is also important the regularity of its contour [11].

In this context, a method aimed at automatically segmenting the FAZ is desirable, due to the objectivity and reproducibility properties associated with this type of method. There are several approaches in the literature that identify and segment the FAZ in different retinal image modalities. For example, there exist methods for the FAZ segmentation in retinography images [12], [13]. In other cases, the FAZ identification method is also used to obtain the DR degree [14], [15]. There are also other studies where the FAZ is segmented in images obtained by fluorescein angiography [16], an invasive image modality that allows the experts a better visualization of the retinal vessels and FAZ than with traditional retinography.

However, given the novelty of the OCT-A imaging, there are few computational studies based on the automatic extraction of the FAZ in this new image modality. Most of them are based on semi-automatic approaches. For example, Lu *et al.* [17] introduced a semi-automatic approach to extract the FAZ region and used this result to classify images in healthy or diabetic subjects. Specifically, a manual initialization placed a seed on the center of the FAZ region and, then, region growing and morphological operators were applied to this seed to obtain the final FAZ region. Similarly, Alam *et al.* [18] proposed a semi-automatic approach, where the FAZ contour was semi-automatically demarcated and the FAZ was segmented using an active contour model, being the seed point manually placed at the center of the fovea. Meanwhile, Eladawi *et al.* [19] implemented an automatic method to

perform the early detection of DR using different biomarkers: the blood vessels density, the retinal vascular appearance and the distance map of the FAZ (map that shows the Euclidean distance between each pixel in the segmented FAZ area and its nearest boundary pixel). In particular, for obtaining the last biomarker, the authors carried out a semi-automatic extraction of the FAZ: the fovea center is manually selected as a seed that is used by region growing techniques and morphological operators with the final objective of segmenting the FAZ. Finally, in a different way, Díaz *et al.* [20] proposed the first fully automatic method to extract the FAZ and it works as follows. First, the largest dark blob in the image is localized (it is assumed that this region always corresponds to the FAZ). Then, the localization blob is used as a seed to apply region growing techniques to precisely extract the FAZ contour.

In this work, we propose a three-stage approach to automatically identify the FAZ in OCT-A images. The first stage generates two FAZ normality models: one of them characterizes the superficial plexus and, the other, the deep plexus. The second stage uses cross-correlation-based adaptive template matching to precisely and robustly localize the FAZ. The OCT-A image and FAZ model play the role of *frame* and *template*, respectively. The template matching applied is said adaptive because the best-scaled template is automatically chosen for each analyzed image. Finally, the third stage uses global adaptive binarization for segmenting the FAZ. Specifically, the implemented segmentation method exploits different binarization thresholds oriented to find an optimum segmentation that minimizes the root mean square error between two sub-windows: the first one is centered in the FAZ center of the input OCT-A image and the second one contains two types of pixels that result of binarizing and processing the first sub-window. Additionally, to reduce the computational cost and noise, the three stages are applied using a resolution lower than the original resolution of the OCT-A images stored in the database used.

The rest of the manuscript is organized as follows: Section II describes the features of the two OCT-A image subsets used in the different experiments. Section III explains in detail the approach that was proposed for modeling, localizing, and segmenting the FAZ region. Section IV shows and analyzes the results obtained in the experiments performed to validate our approach. Finally, Section V exposes the main conclusions of this work.

II. MATERIALS

To validate the proposed method, we used two public subsets of images belonging to the denominated OCTAGON database (version 2) [21]. In this database, all the images were taken using the optical coherence tomography capture device *DRI OCT Triton* at the typical configurations: two different levels of zoom (3×3 mm^2 and 6×6 mm^2) and depths (*superficial* and *deep*), and with a resolution of 320×320 pixels.

The first subset, also known in the literature as OCTAGON database (version 1) or, simply, the OCTAGON database, contains 213 OCT-A images (144 healthy and 69 with diabetic retinopathy) grouped into different categories. The FAZ in the images belonging to the ''healthy'' category was manually labeled and segmented by two expert clinicians (*expert#1* and *expert#2*) and, in the case of the ''diabetic retinopathy'' category, by just one expert. Table 1 summarizes the number of images belonging to each category. A more detailed description of this subset of images can be consulted in [20].

TABLE 1. The number of images belonging to each category in the first subset of the OCTAGON database (version 2).

	3×3 mm^2		6×6 mm^2	
	superficial	deep	superficial	deep
Healthy	36	36	36	36
Diabetic retinopathy	19	17	17	16

The second subset contains 48 OCT-A images in which the task of localizing and segmenting the FAZ is much harder than the first subset. Three circumstances in this dataset can difficult the automatic identification of the FAZ: (i) the presence of ischemic areas, where blood circulation has decreased or stopped, can increment the number of false positives; (ii) the existence of different artifacts can lead to the misidentification of the FAZ, especially if some of these artifacts are dark or located within the FAZ; and (iii) the handling of OCT-A images not centered in the FAZ can be a great challenge since there are localization or segmentation methods that assume that the image is always centered in the FAZ. Table 2 summarizes the number of images belonging to each category. In this subset, only one expert clinician manually segmented the FAZ region of each image.

TABLE 2. The number of images belonging to each category in the second subset of the OCTAGON database (version 2).

	3×3 mm^2		6×6 mm^2	
	superficial	deep	superficial	deep
With ischemia	2	6	6	6
With artifacts	2	2	3	7
Not centered in the FAZ	0	0	8	6

III. METHOD DESCRIPTION

The complete description of the proposed method implies three main stages. The first is dedicated to generating two representative FAZ normality models (3×3 mm^2): one of them is associated with the superficial capillary plexus and, the other, with the deep capillary plexus. Then, a template matching-based method uses the superficial or deep FAZ model as a template to localize the FAZ in superficial or deep plexus images (independently of the level of zoom), respectively. Finally, using the FAZ localization information, a method based on adaptive binarization is applied to precisely segmenting the entire FAZ region. In this section, each one of these stages is described in detail.

A. GENERATING FAZ NORMALITY MODELS

This section describes how to create a FAZ normality model for later use as a template in the FAZ localization method. Specifically, we created two FAZ normality models, considering the superficial and deep plexus, and both of them with a level of zoom of 3×3 mm^2. To do so, each model was calculated as the average intensity of N square sub-windows centered in the FAZ. We only used the images belonging to the "healthy" category of the first subset of images (see Section II). In particular, each sub-window has a width of $L \times L$, being centered in the actual FAZ center and extracted from each 3×3 mm^2 image, $\mathbf{I}_i$, which is previously scaled with a factor scale α_i defined as:

$$\alpha_i = K \cdot \sqrt{\frac{\overline{A}}{A_i}}, \tag{1}$$

where $\overline{A}$ is the average FAZ area (calculated from the FAZ of N "healthy" images), A_i is the FAZ area corresponding to the current image, and K is called the *work scale* and is given by:

$$K = 1/2^q \tag{2}$$

being $q \in \mathbb{N}$. The reduction of the image size that results in applying the work scale, K, helps to decrease the image processing time and also to eliminate some noisy artifacts that are present in the original image. Additionally, the term $\sqrt{\overline{A}/A_i}$ in Eq. (1) allows us to slightly readjust the size of each image to ensure that the size of the FAZ is similar in all the sub-windows considered to calculate the model. For example, if $A_i > \overline{A}$, the value of α_i will be slightly smaller than K, and the size of the FAZ will decrease slightly before contributing to the calculation of the mean. On the contrary, if $A_i < \overline{A}$, then α_i will be slightly larger than K and the size of the FAZ will increase conveniently.

Algorithm 1 shows the steps that are followed to obtain the superficial plexus FAZ model. A similar procedure was used to obtain the deep plexus FAZ model. The only difference is that 3×3 mm^2 superficial plexus healthy images were just used in the construction of the superficial model and 3×3 mm^2 deep plexus healthy images were used in the deep model. Although the OCT-A images are gray-scale images, they are stored in the TIFF file format with three channels, where each channel has the same information. Therefore, we use the RGB-to-grayscale operator to highlight the presence of the three channels in the input image, but the result obtained by this operator is the same as selecting one of the three channels.

The values of the parameters used to build both models (see Algorithm 1) were the following: $N = 36$, that is, all the "healthy" images (superficial or deep) of the first subset of images with the level of zoom 3×3 mm^2 were used (see Table 1). The exponent used to calculate the work scale was $q = 2$. This value is high enough to reduce the image size and to eliminate some artifacts that are present at higher sizes, as well as low enough so that the FAZ does not loose details

Algorithm 1 Pseudo-Code to Obtain the Superficial Plexus FAZ Model (3×3 mm^2)

Inputs

$\mathbf{I}_{RGB} = \{\mathbf{I}_1, \ldots, \mathbf{I}_N\}$, superficial plexus healthy imgs (3×3 mm^2)

$\mathbf{C} = \{\mathbf{C}_1, \ldots \mathbf{C}_N\}$, FAZ centers of superf. plexus healthy imgs (3×3 mm^2)

$\mathbf{A} = \{A_1, \ldots, A_N\}$, FAZ areas in superf. plexus healthy imgs (3×3 mm^2)

q, exponent to calculate the work scale ($K = 1/2^q$)

m, m-by-m neighborhood used by the median filter

L, sub-window size ($L \times L$)

Output

$\mathbf{M_{FAZ}}$, superficial plexus FAZ model (3×3 mm^2)

1: $\overline{A} \leftarrow$ `mean`$(A_1, .., A_N)$
2: **for** $i \leftarrow 1$ **to** N
3: $\quad \alpha_i \leftarrow K \cdot \sqrt{\overline{A}/A_i}$;
4: $\quad \mathbf{C}' \leftarrow$ `scale-center` $(\mathbf{C}_i, \alpha_i)$;
5: $\quad \mathbf{I}_g \leftarrow$ `RGB-to-grayscale` $(\mathbf{I}_i)$;
6: $\quad \mathbf{I}'_g \leftarrow$ `resize-image` $(\mathbf{I}_g, \alpha_i)$;
7: $\quad \mathbf{I}_n \leftarrow$ `normalize-image` $(\mathbf{I}'_g)$;
8: $\quad \mathbf{I}_m \leftarrow$ `median-filter` $(\mathbf{I}_n, m)$;
9: $\quad \mathbf{W_{FAZ}}(i) \leftarrow$ `extract-FAZ-subwindow` $(\mathbf{I}_m, \mathbf{C}', L)$;
10: **end-for**
11: $\mathbf{M_{FAZ}} \leftarrow$ `mean` $(\mathbf{W_{FAZ}}(1), \ldots, \mathbf{W_{FAZ}}(N))$;
12: $\mathbf{M_{FAZ}} \leftarrow$ `median-filter` $(\mathbf{M_{FAZ}}, m)$;

of interest (taking into account that 3×3 mm^2 OCTAGON images have a resolution of 320×320 pixels); the size of $m \times m$ neighborhood used by the median filter was set to $m = 5$ (at the work scale), considering that was a reasonable size to indirectly produce the following actions: (i) blur the vessels, (ii) preserve the typical pattern of contour lines of the FAZ periphery, and (iii) eliminate the typical salt&pepper noise associated with the FAZ in this image modality. Finally, the value that was chosen for the sub-window size, $L = (2 \times \overline{D}) + 1$, was high enough to include the FAZ and its periphery, being $\overline{D}$ the average FAZ diameter in pixels. To use the maximum range of gray intensity, a normalization based on contrast stretching was applied, where the bottom and top 1% of all the pixel values are saturated to 0 and 255, respectively. The values of FAZ areas, $A_1, \ldots, A_N$, and FAZ centers, $C_1, \ldots, C_N$, were obtained from the expert#1.

Figures 3.a-b show the two obtained gray-level models. It can be seen (and computed) that the average FAZ area associated with the deep plexus (289.5 ± 83.9 pixels) is greater than that associated with the superficial plexus (226.7 ± 65.3 pixels). This result is consistent with other related studies in the literature [22], [23]. Additionally, Figs. 3.c-d show the contour plots of each model. It can be seen that all the contour lines (isolines) in the periphery of an average healthy FAZ are nested (assuming that blood vessels are blurred), the intensity

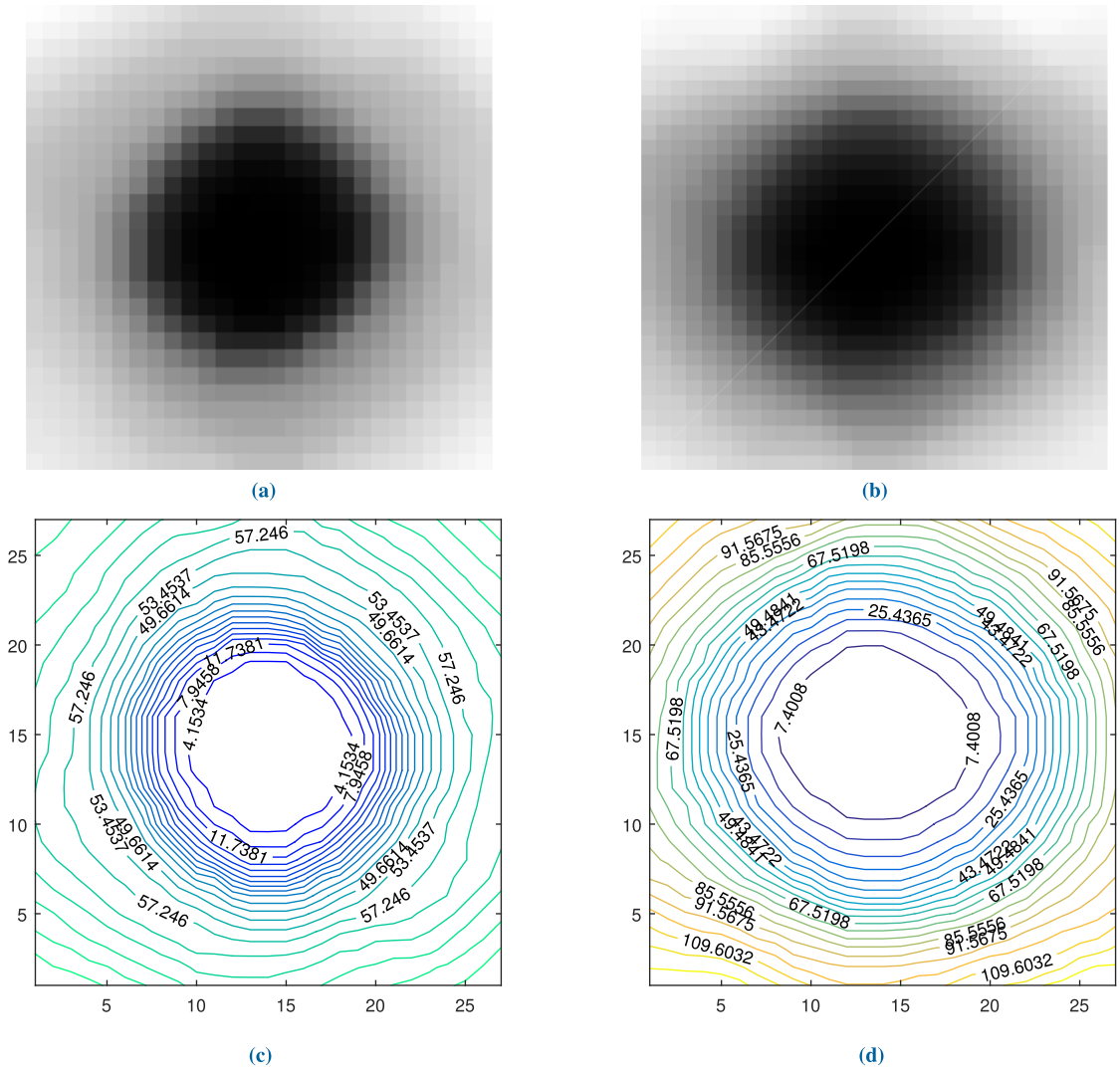

FIGURE 3. The two FAZ normality models (3×3 mm^2) at work scale: (a) the superficial plexus model (gray-level); (b) the deep plexus model (gray-level); (c) the contour plot of the superficial plexus model; and (d) the contour plot of the deep plexus model.

of the image grows from the FAZ center towards its periphery and the slope of the intensity growth in the deep plexus is greater than that corresponding to the superficial plexus.

Finally, note that to obtain the superficial and deep FAZ normality model at work scale and for a level of zoom 6×6 mm^2, it will be enough to resize its respective 3×3 mm^2 model, using a scale factor equal to $1/2$. As will be seen in Section IV, the generation of these normality models will provide stability and robustness to the localization method, not only facilitating the FAZ identification in normal cases but also, and especially, in the most complex scenarios (with presence of noise, artifacts or pathological FAZ).

B. FAZ LOCALIZATION STAGE

Using the FAZ model as a reference, the FAZ localization is done using cross-correlation-based adaptive template matching [24], [25]. In general, template matching (TM) is the process of finding the position(s) at which a specified template is located inside an image frame (search area of a larger size than the template). Specifically, the matching process involves the following steps: (i) the template is shifted from left to right and from top to bottom within the frame, (ii) at each template location, the similarity between the template and the frame sub-window covered by the template is computed, and (iii) those positions that obtain a high similarity are stored. Although mean absolute error or other similar error measurements have been used to compute the similarity, the advantages of using correlation are its reliability and accuracy [26]. Specifically, the correlation coefficient is independent of any offset or linear transformation in the set of pixel values to compare and, if we compute its normalized version, its value will always be bounded in the interval $[-1, 1]$.

In the TM context, we use the OCT-A image as the frame, and the FAZ model, associated with the OCT-A image type (superficial or deep), as the template. Previously, it is

necessary to make two considerations. First, before applying TM, we have to apply to the image input the same preprocessing steps that were used to build the FAZ model: (i) RGB-to-grayscale, (ii) resize to the work scale, (iii) normalize, and (iv) median filter. Second, it must be noted that the FAZ of each patient's eye may be slightly different in size from our FAZ model. Therefore, we apply an adaptive TM, where different sizes of the original FAZ model (template) are used. For each template scale, the TM produces a matrix of intensity levels with the property of having high-intensity values where the degree of matching is high. However, due to the existence of noise and other artifacts in the image, the TM output can include one or more zones (blobs) with high response. To count the number of blobs that present this property, we binarize the TM output obtained for each template size, using a threshold that represents a percentage of the maximum correlation value that was obtained. This percentage is predefined empirically. Finally, the FAZ center is selected as the pixel of maximum correlation, considering only those correlation matrices (one or more) where the number of maximum correlation blobs was minimum (ideally, one blob per matrix).

Algorithm 2 summarizes the different steps followed to localize the FAZ in 3×3 mm^2 superficial plexus images. Note that, in each iteration of the "for" loop, a different scale is applied to the template; additionally, the FAZ center, $\mathbf{C}_{FAZ}$, and the maximum correlation value, MAX_{CORR}, are just updated when the number of maximum correlation blobs obtained is: (i) less than that obtained in any previous iteration, independently of the maximum correlation reached until now; or (ii) equal to the minimum number of maximum correlation blobs obtained until now and the maximum correlation obtained in the iteration is greater than or equal to that stored in MAX_{CORR}. A similar algorithm could be used to localize the FAZ in 3×3 mm^2 deep plexus images. The only difference is that the input image and the FAZ model would be associated with the 3×3 mm^2 deep plexus. Similarly, the described algorithm could be used to localize the FAZ in 6×6 mm^2 deep and superficial plexus images: the only consideration to take into account is that the original resolutions of the 3×3 mm^2 and 6×6 mm^2 OCT-A images are equal (see Section II). Therefore, in the case of 6×6 mm^2 OCT-A images, the value of exponent used to calculate the work scale has to be set to $q = q' - 1$, being $q' = 2$ the value used to calculate the FAZ model.

The values of the parameters used to localize the FAZ (see Algorithm 2), considering the different configurations in the OCTAGON database, were the following: the parameter values related to the preprocessing stage, m and q, were equals to those used to build the FAZ models (see Section III-A). Here, as already mentioned above, the only exception is the value of parameter q for the case of 6×6 mm^2 images, which is set to $q = 1$ ($q = 2$ for 3×3 mm^2 images). The template scale is varied from 0.5 to 1.5 times the original size of the FAZ model, using a step size equal to 0.1 (see *ScaleSet* parameter). Finally, the percentage of the maximum correlation value was set to $Th_{\%} = 0.75$. The tuning of this parameter was made by trial and error, but it is not critical, that is, other values close to the chosen value work adequately.

Algorithm 2 Pseudo-Code to Localize the FAZ in 3×3 mm^2 Superficial Plexus Images. To Adapt This Algorithm to 3×3 mm^2 Deep, 6×6 mm^2 Superficial or 6×6 mm^2 Deep Plexus Images, See Section III-B

Inputs
- $\mathbf{I}_{RGB}$, 3×3 mm^2 superficial plexus image
- $\mathbf{M}_{FAZ}$, superficial plexus FAZ model
- q, exponent to calculate the work scale
- m, m-by-m neighborhood used by the median filter
- *ScaleSet*, set of values to scale the template
- $Th_{\%}$, percentage of maximum correlation value

Output
- $\mathbf{C}_{\mathbf{FAZ}}$, FAZ center

```
MAX_CORR ← −1;
N_BLOBS ← ∞;
K ← 1/2^q;
Frame ← preprocess (I_RGB, K, m);
for TemplateScale ∈ ScaleSet
  Template ← resize-template (M_FAZ, TemplateScale);
  M_TM ← template-matching (Frame, Template);
  max ← max(M_TM);
  Th ← Th_% × max;
  M_b ← binarize (M_TM, Th);
  n_blobs ← count-blobs (M_b);
  if n_blobs < N_BLOBS
    N_BLOBS ← n_blobs;
    MAX_CORR ← max;
    C_FAZ ← extract-coordinates(M_TM, MAX_CORR);
  end-if
  if (n_blobs = N_BLOBS) ∧ (max ≥ MAX_CORR)
    MAX_CORR ← max;
    C_FAZ ← extract-coordinates(M_TM, MAX_CORR);
  end-if
end-for
C_FAZ ← scale-center (C_FAZ, 1/K);
```

Figure 4 shows different steps of interest related to the localization stage. Specifically, Fig. 4.a shows the result of preprocessing the input image (frame) at the work scale. In this case, the original input image corresponds to a 3×3 mm^2 superficial healthy OCT-A image. Figure 4.b shows a plot where each point represents the maximum correlation value (y-axis) of the correlation matrix obtained when the template matching uses a template resized with a scale given (x-axis). Figure 4.c shows the optimal size template that was automatically selected. Figure 4.d shows the correlation

matrix at work scale obtained by template matching using the template of optimal size. The result of binarizing the correlation matrix of Fig. 4.d is shown in Fig. 4.e, where just one blob appears. Finally, the FAZ center is obtained from the pixel coordinates of the maximum correlation in the correlation matrix of Fig. 4.d. However, these coordinates are expressed at the work scale. Therefore, they have to be transformed at the original scale, as shown in Fig. 4.f.

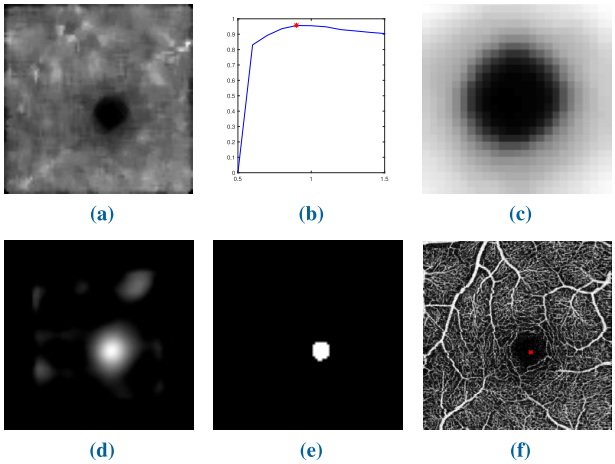

FIGURE 4. Different steps related to the localization stage (see Section III-B for more information): (a) preprocessed input image (frame) at work scale (80 × 80 pixels); (b) plot of maximum correlation value *vs.* template scale; (c) optimum size template (25 × 25 pixels); (d) correlation matrix obtained by template matching and using the optimum size template (80 × 80 pixels); (e) binarized correlation matrix where one blob only appears (80 × 80 pixels); (f) FAZ center on the original input image at original scale (320 × 320 pixels).

Algorithm 3 Pseudo-Code to Segment the FAZ in OCT-A Images

Inputs:
$\mathbf{I}_{RGB}$, OCT-A image
q, exponent to calculate the work scale
m, m-by-m neighborhood used by the median filter
$\mathbf{C}_{FAZ}$, FAZ center of $\mathbf{I}_{RGB}$
w, size of sub-window ($w \times w$)
ThresholdSet, set of thresholds to binarize the sub-window
Output:
FAZ, FAZ segmented

$ERROR \leftarrow \infty$;
$K \leftarrow 1/2^q$;
$\mathbf{I} \leftarrow$ `preprocess` $(\mathbf{I}_{RGB}, K, m)$;
$\mathbf{W}_{FAZ} \leftarrow$ `extract-subwindow` $(\mathbf{I}, \mathbf{C}_{FAZ}, w, m)$;
$\overline{x} \leftarrow \text{mean}(\mathbf{W}_{FAZ})$;
for $Th \in ThresholdSet$
  $\mathbf{W}^b_{FAZ} \leftarrow$ `binarize` $(\mathbf{W}_{FAZ}, Th)$;
  $\mathbf{W}_{tmp} \leftarrow \overline{x} \cdot \mathbf{W}^b_{FAZ}$;
  $error_i \leftarrow \text{RMSE}(\mathbf{W}_{FAZ}, \mathbf{W}_{tmp})$;
  if $error_i < ERROR$
    $ERROR \leftarrow error_i$;
    $\mathbf{S}_{FAZ} \leftarrow \mathbf{W}^b_{FAZ}$;
  end-if
end-for
$\mathbf{FAZ}_{tmp} \leftarrow$ `resize-to-original-scale` $(\mathbf{S}_{FAZ}, 1/K)$;
$\mathbf{FAZ} \leftarrow$ `postprocess` $(\mathbf{FAZ}_{tmp})$;

C. FAZ SEGMENTATION STAGE

The FAZ segmentation is carried out using an adaptive binarization process applied to an image sub-window centered in the FAZ center. In this context, the optimum binarization threshold will produce a binary image where the pixels corresponding to the actual FAZ region present value zero, and the rest of the pixels present values equal to 1. There exists in the literature different binarization techniques [27], [28], but we propose here a global adaptive binarization method that was adapted to segment the FAZ region. Specifically, Algorithm 3 shows the procedure in pseudo-code. First of all, a preprocessing stage is applied to the input OCT-A image, $\mathbf{I}_{RGB}$, that includes the same steps as the localization preprocessing stage: (i) RGB-to-grayscale, (ii) resize to the work scale, (iii) normalize, and (iv) median filter. Next, a sub-window, $\mathbf{W}_{FAZ}$, centered in the FAZ center, $\mathbf{C}_{FAZ}$, is extracted from the preprocessed image, $\mathbf{I}$. We assume that the FAZ center is obtained as a result of applying our localization algorithm (see Section III-B). However, any other localization method could be used. Then, an iterative process of binarization is applied to $\mathbf{W}_{FAZ}$. In each iteration, a different binarization threshold, belonging to a set of possible values, is used. In order to evaluate each FAZ sub-window segmentation result, $\mathbf{W}^b_{FAZ}$, obtained for each binarization threshold, we apply the following procedure: $\mathbf{W}^b_{FAZ}$ is multiplied by the mean value of $\mathbf{W}_{FAZ}$, denoted by $\overline{x}$, obtaining $\mathbf{W}_{tmp}$, and then the root mean square error (RMSE) is calculated between $\mathbf{W}_{FAZ}$ and $\mathbf{W}_{tmp}$. The hypothesis of the segmentation method is the following: the binarization that produces the best approximation to the actual FAZ segmentation will also return the smallest RMSE.

To clarify our segmentation hypothesis, we can consider three scenarios clearly differentiated, depending on the binarization threshold value: (i) it is too large; (ii) it is too small; and (iii) it is close to the optimum value. In particular, Fig. 5 illustrates each of these scenarios. Thus, using a very large threshold, almost all the pixels of the preprocessed sub-window (Fig. 5.a) are binarized to zero (Fig. 5.b), that is, almost all the pixels are considered as belonging to the FAZ. Then, the multiplication by $\overline{x}$ produces a matrix $\mathbf{W}_{tmp}$ with almost all its elements equal to zero (Fig. 5.c) and, therefore, practically all the pixels, except those that actually belong to the FAZ region, will contribute to increasing the RMSE (Fig. 5.d). Conversely, the use of a very small threshold makes that almost all the pixels of the sub-window are binarized to 1 (Fig. 5.e); now, the multiplication by $\overline{x}$ produces a matrix $\mathbf{W}_{tmp}$ with almost all its elements equal to $\overline{x}$ (Fig. 5.f) and, therefore, those elements that actually belong to the FAZ,

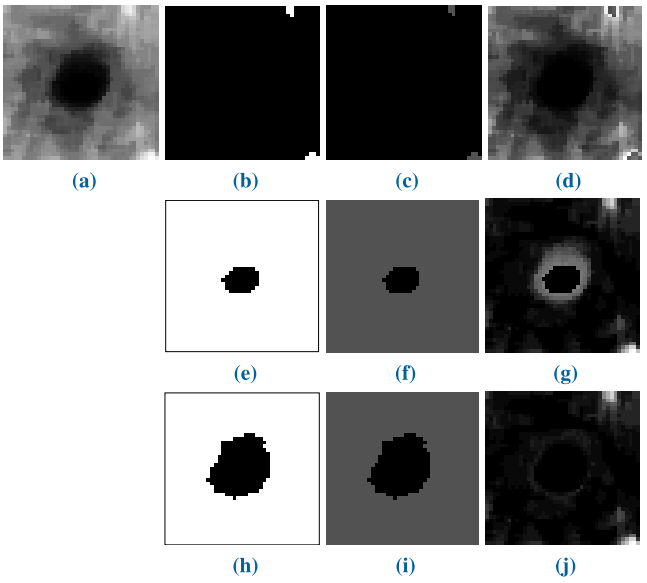

FIGURE 5. Three FAZ segmentation scenarios (rows) based on the binarization threshold value (see Section III-C for more details): (a) sub-window centered in the FAZ ($\mathbf{W}_{FAZ}$); (b), (e) and (h) matrices resulting ($\mathbf{W}^{b}_{FAZ}$) from applying a maximum, minimum and near optimal binarization threshold value to $\mathbf{W}_{FAZ}$, respectively; (c), (f) and (i) matrices resulting ($\mathbf{W}_{tmp}$) from multiplying the scalar $\bar{x} = \text{mean}(\mathbf{W}_{FAZ})$ and the matrix obtained in (b), (e) and (h), respectively; (d), (g) and (j) error matrices resulting from calculating $\mathbf{W}_{error} = (\mathbf{W}_{FAZ} - \mathbf{W}_{tmp})^2$, where $\mathbf{W}_{tmp}$ is obtained from (c), (f) and (i), respectively. Note that, in the matrices $\mathbf{W}_{error}$ (last column), a greater intensity level implies a greater error.

but have not been labeled correctly, will contribute mainly to increase the RMSE (Fig. 5.g). Finally, the use of the optimum threshold, or close to the optimum, makes that those pixels actually belonging to the FAZ region are binarized to zero, and the remaining pixels are binarized to 1 (Fig. 5.h). The multiplication by $\bar{x}$ produces a matrix $\mathbf{W}_{tmp}$ with elements associated with the actual FAZ equal to zero and with the remaining elements equal to $\bar{x}$ (Fig. 5.i); this is the case in which the contribution to the RMSE will be minimal: the elements equal to zero (FAZ pixels) will not contribute practically to the error and the remaining elements, whose value are equal to $\bar{x}$, will contribute minimally to the error (Fig. 5.j).

Note that Algorithm 3 can be used without any change with deep and superficial plexus OCT-A images and with both levels of zoom. The only particularity is that the exponent to calculate the work scale is set to $q = 1$ for the level of zoom 6×6 mm^2 and $q = 2$ when the level of zoom 3×3 mm^2 is considered. This is because the OCT-A image resolution for both levels of zoom is the same (see Section II). The values used for the preprocessing parameters are the same as those used in the FAZ localization (see Section III-B). The size of the sub-window, $w \times w$, defined at the work scale was set to $w = L + 14$, where $L \times L$ is the size of the template used in the localization stage. The idea is that, in the calculation of the mean value, $\bar{x}$, there were much more retina background pixels than FAZ pixels in the sub-window. In any case, the chosen sub-window size is not critical and any other similar value could have been chosen. The *ThresholdSet* parameter varies from 0 to 0.5 with a step of 0.01 (values belonging to the interval (0.5, 1] were not utilized because they always guaranteed the largest RMSE values). Additionally, the FAZ segmentation includes a post-processing stage that implies the following sequence of steps: (i) elimination of holes; (ii) selection of the blob of the maximum area; (iii) eroding image; (iv) selection of the blob of the maximum area; (v) dilating image. The justification for these steps is as follows. The step (i) eliminates possible holes in the FAZ blob. The step (ii) assumes that, if the binarization process produces two o more blobs, the largest will correspond to the FAZ blob. Finally, the objective of the steps (iii) - (v) is to eliminate the possible appearance of noisy artifacts in the form of small appendages protruding from the FAZ blob.

IV. RESULTS AND DISCUSSION

We conducted different experiments to validate the proposed localization and segmentation method using the two image subsets belonging to the public dataset described in Section II. With the first subset, we compare our results to the manual labeling of each expert clinician and to the results obtained in [20], considering the different levels of complexity associated with the six possible configuration criteria (deep or superficial plexus, two levels of zoom, and healthy *vs*. diabetic retinopathy). With the second subset, we are more interested in the behavior of the localization and segmentation method in each category of difficulty (images with ischemia, with artifacts or not centered in the FAZ), comparing the results obtained with those labeled by the expert.

A. LOCALIZATION RESULTS

To evaluate the FAZ localization method, we consider that a localization result was successful if the obtained FAZ center is placed inside the manual segmentation of the expert clinician. Besides, we provide the average distance considering the obtained FAZ centers and the expert FAZ centroids. Note that, in [20], a localization result is successful if the obtained FAZ blob centroid is placed inside the expert manual segmentation, and the average distance is calculated considering the obtained blob centroids and the expert FAZ segmentation centroids. Hereinafter, the two mentioned average distances will be called the *average inter-centroid distances*. Tables 3 and 4 show the localization results obtained in the first subset of the OCTAGON database for the ''healthy'' and ''diabetic'' images, respectively. As can be seen, our success rate (SR) is equal to 100% in all the considered scenarios. Comparing our method with the localization method used in [20], the results are very similar. There is only a slight difference in the case of 6×6 mm^2 superficial healthy OCT-A images, where the SR in the second method drops to 88.9% (for expert#1 and expert#2). In addition, if we consider the total number of images in the mentioned subset, our SR is 100% *vs*. 98.1% (four wrong localizations) in the method implemented by Díaz *et al*. On the other hand, about the average

TABLE 3. Results of the FAZ localization success rate (SR) and the average inter-centroid distance (D) calculated for the "healthy" images in the first subset of the OCTAGON database (version 2). The standard deviation (SD) is also included. The best result in the comparison for each configuration and method is highlighted in bold.

Level of zoom	Method	Superficial		Deep	
		SR (%)	D±SD (mm)	SR (%)	D±SD (mm)
3×3 mm^2	Expert#1 *vs*. Expert#2	–	0.02 ± 0.01	–	0.06 ± 0.03
	Method [20] *vs*. Expert#1	100	$\mathbf{0.02 \pm 0.01}$	100	$\mathbf{0.04 \pm 0.02}$
	Proposed method *vs*. Expert#1	100	0.03 ± 0.02	100	0.05 ± 0.03
	Method [20] *vs*. Expert#2	100	$\mathbf{0.02 \pm 0.01}$	100	0.04 ± 0.02
	Proposed method *vs*. Expert#2	100	0.03 ± 0.02	100	0.04 ± 0.02
6×6 mm^2	Expert#1 *vs*. Expert#2	–	0.06 ± 0.03	–	0.07 ± 0.03
	Method [20] *vs*. Expert#1	88.9	0.07 ± 0.04	88.9	$\mathbf{0.07 \pm 0.04}$
	Proposed method *vs*. Expert#1	**100**	$\mathbf{0.06 \pm 0.03}$	**100**	0.09 ± 0.04
	Method [20] *vs*. Expert#2	88.9	0.05 ± 0.09	88.9	0.05 ± 0.03
	Proposed method *vs*. Expert#2	**100**	$\mathbf{0.05 \pm 0.03}$	**100**	0.05 ± 0.03

TABLE 4. Results of the FAZ localization success rate (SR) and the average inter-centroid distance (D) calculated for the "diabetic" images in the first subset of the OCTAGON database (version 2). The standard deviation (SD) is also included. The best result in the comparison for each configuration and method is highlighted in bold.

Level of zoom	Method	Superficial		Deep	
		SR (%)	D±SD (mm)	SR (%)	D±SD (mm)
3×3 mm^2	Method [20]	100	$\mathbf{0.01 \pm 0.01}$	100	$\mathbf{0.05 \pm 0.04}$
	Proposed method	100	0.04 ± 0.02	100	0.07 ± 0.07
6×6 mm^2	Method [20]	100	$\mathbf{0.05 \pm 0.04}$	100	0.13 ± 0.30
	Proposed method	100	0.07 ± 0.04	100	$\mathbf{0.11 \pm 0.12}$

inter-centroid distance, the results are also very similar when both approaches are compared and, the most important, they are also similar compared to the average distance between both experts (see Table 3). In summary, we can say that our localization method has adequate performance in typical scenarios where previous approaches were also satisfactory.

Additionally, for evaluating our method in a more challenging scenario, we used the second subset of images, which includes more complex and challenging conditions (see Section II). Table 5 includes the obtained localization results. In this case, we only show the SR and the average inter-centroid distance for each indicated category, since the value of these two parameters for the other criteria (zoom or depth levels) could produce results that are not statistically significant, given the low number of images associated with some of these criteria (zero in some cases). Therefore, considering the total number of images in this subset, we obtain a SR and average inter-centroid distance of 95.8% and 0.13 ± 0.19 mm, respectively. The errors only appear in two images belonging to the category "images with ischemia" and the rest of the images are successfully localized. Note that the most penalized average distance also corresponds to the mentioned category. On the other hand, the images not centered in the FAZ have an average distance and standard deviation very similar to those shown in Tables 3 and 4. This result evidences that the performance of our localization method does not depend on the position of the FAZ in the input image. Fig. 6 shows some localization examples in this complex image subset.

TABLE 5. Results of the FAZ localization success rate (SR) and the average inter-centroid distance (D) calculated for the images in the second subset of the OCTAGON database (version 2). The standard deviation (SD) is also included.

Category	SR (%)	D±SD (mm)
With ischemia	90.0	0.19 ± 0.26
With artifacts	100	0.10 ± 0.12
Not centered in the FAZ	100	0.06 ± 0.05
All the images	95.8	0.13 ± 0.19

Finally, taking into account both subsets of images, the localization SR of our method is 99.2%. We think that this global result is good enough to consider our localization method as an alternative to the initialization phase used in some semi-automatic methods where a point inside the FAZ has to be manually selected [17]–[19]. Furthermore, given that our localization method is based on a model, it works well without assuming that the FAZ has to be centered [17], [19], [20] or is the larger avascular zone in the image [20]. Note that the presence of a large dark or avascular area may be associated with the presence of an artifact or ischemia, respectively, and not necessarily with the FAZ. Summarizing, the proposed localization method, based on a robust and versatile FAZ model, takes advantage of the characteristics of the FAZ region and offers satisfactory results, not only in normal and typical conditions but also in those challenging, noisy and pathological scenarios that are frequent in clinical practice.

B. EVALUATING THE ROBUSTNESS OF THE LOCALIZATION METHOD

An interesting aspect of working with two OCT-A images of the same patient's eye with two different levels of zoom (3×3 mm^2 and 6×6 mm^2) is that it is possible to consider the idea of comparing the FAZ centers obtained in each level

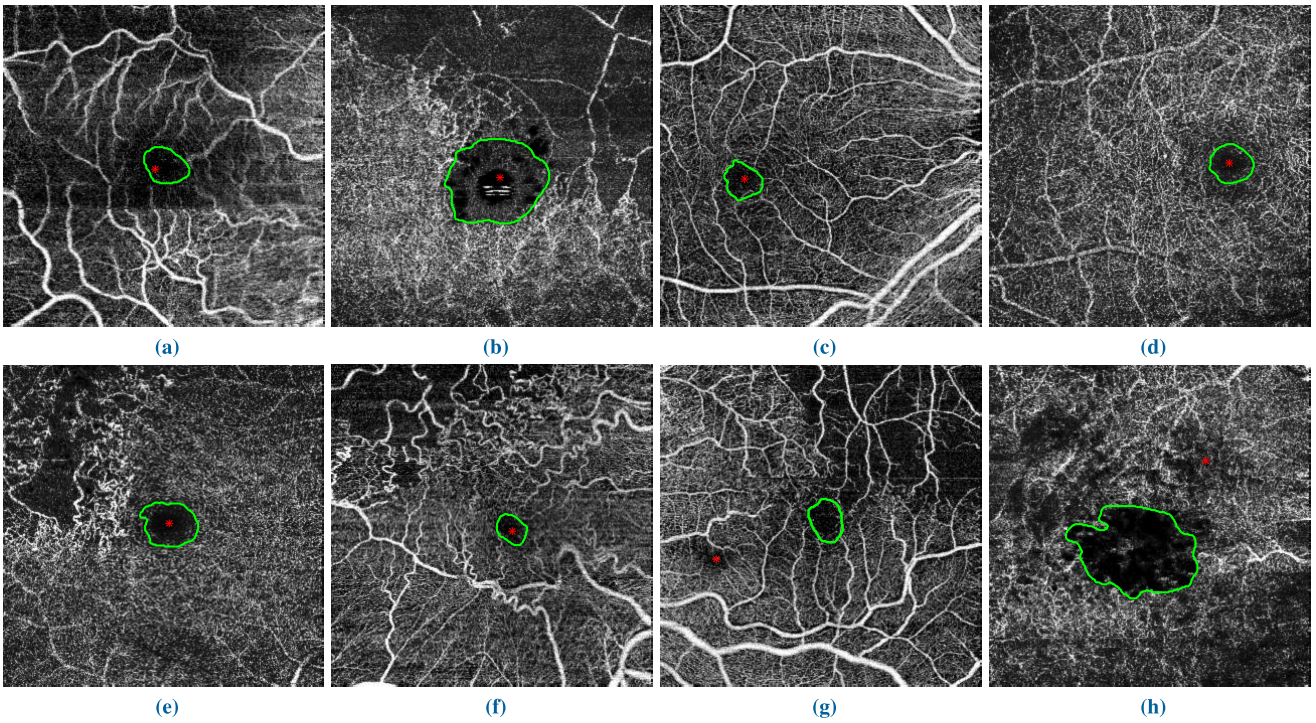

FIGURE 6. Examples of localization results in the more complex subset of the OCTAGON database (version 2): (a)-(b) images with artifacts; (c)-(d) images not centered in the FAZ; (e)-(f) images with ischemia (successful localization); (g)-(h) images with ischemia (wrong localization).

of zoom. Thus, if the distance obtained between both centers is close, the automatic FAZ localization system can give more credit to the obtained localization results. However, the comparison of these two FAZ centers cannot be made directly, since the origin of the coordinate system of each of them is different. In order to solve this inconvenience, we again utilize correlation-based template matching. In this case, the 3×3 mm^2 OCT-A image is considered as the template and, the 6×6 mm^2 OCT-A image, as the frame. Algorithm 4 summarizes the steps proposed to carry out the comparison. First, a preprocessing stage is applied in order to reduce the effect of noise and other artifacts. This stage includes the same steps as those used in the localization stage: (i) RGB-to-grayscale, (ii) resize to the work scale, (iii) normalize, and (iv) median filter. Here, the exponent used to calculate the work scale in each image depends on the exponent used to obtain the FAZ center in each level of zoom, that is, $q_{3\times3} = 2$ for the 3×3 mm^2 images and $q_{6\times6} = q_{3\times3} - 1$ for the 6×6 mm^2 images. Then, assuming that template matching produced maximum correlation in position (x_0, y_0) and the FAZ center coordinates obtained in the localization stage for the corresponding 3×3 mm^2 and 6×6 mm^2 OCT-A images were $\mathbf{C}_{3\times3} = (x_{3\times3}, y_{3\times3})$ and $\mathbf{C}_{6\times6} = (x_{6\times6}, y_{6\times6})$, respectively, then the FAZ center, $\mathbf{C}'_{3\times3}$, of the 3×3 mm^2 OCT-A image referred to the coordinate system of the 6×6 mm^2 OCT-A image will be:

$$\begin{aligned} x'_{3\times3} &= x_0 + x_{3\times3} \\ y'_{3\times3} &= y_0 + y_{3\times3} \end{aligned} \tag{3}$$

and the distance between $\mathbf{C}'_{3\times3}$ y $\mathbf{C}_{6\times6}$ is now easily computable:

$$D(\mathbf{C}'_{3\times3}, \mathbf{C}_{6\times6}) = \sqrt{(x'_{3\times3} - x_{6\times6})^2 + (y'_{3\times3} - y_{6\times6})^2} \tag{4}$$

Note that the distance expressed by Eq. (4) is finally multiplied by $1/K_6$ in Algorithm 4. The idea is to obtain the distance value at the original scale.

We can compare the FAZ centers obtained by the localization method for the corresponding 6×6 mm^2 and 3×3 mm^2 OCT-A images in each eye. However, this comparison can only be done systematically here for images belonging to the "healthy" category in the first image subset, since only in this case there are pairs of images of the same patient's eye with the two zoom levels. Figure 7 shows the box-plots of the inter-center distances, expressed in mm, for superficial and deep plexus. We can observe that the box-plots are nearly identical, with the only exception of the one distance value that is labeled as an outlier in the box-plot associated with the superficial plexus. The median obtained was 0.038 mm in both cases. To put in context the two obtained distance distributions, we have to take into account that the average FAZ radius is 0.315 and 0.356 mm for superficial and deep OCT-A "healthy" images, respectively. The largest obtained distance corresponds to the outlier (0.191 mm), that is, all the distances are less than any of the two average FAZ radii, even considering the worst case. Therefore, assuming that the FAZ gold standard was unknown, we could trust in the obtained localization results. This hypothesis is confirmed

Algorithm 4 Pseudo-Code to Compute the Distance Between the FAZ Centers of the Corresponding 6×6 mm^2 and 3×3 mm^2 OCT-A "healthy" Images Obtained in the Localization Stage

Inputs

$\mathbf{I}_{6\times6}$, 6×6 mm^2 OCT-A image

$\mathbf{I}_{3\times3}$, 3×3 mm^2 OCT-A image

$q_{3\times3}$, exponent used to calculate the work scale of $\mathbf{I}_{3\times3}$

$\mathbf{C}_{3\times3}$, FAZ center of $\mathbf{I}_{3\times3}$ obtained at work scale ($q_{3\times3}$)

$\mathbf{C}_{6\times6}$, FAZ center of $\mathbf{I}_{6\times6}$ obtained at work scale ($q_{6\times6} = q_{3\times3} - 1$)

m, m-by-m neighborhood used by the median filter

Output

D, distance between FAZ centers $\mathbf{C}_{3\times3}$ and $\mathbf{C}_{6\times6}$ at original resolution

$K_{3\times3} \leftarrow 1/2^{q_{3\times3}}$;
$K_{6\times6} \leftarrow 1/2^{(q_{3\times3}-1)}$;
$Frame \leftarrow$ `preprocess` $(\mathbf{I}_{6\times6}, K_{6\times6}, m)$;
$Template \leftarrow$ `preprocess` $(\mathbf{I}_{3\times3}, K_{3\times3}, m)$;
$\mathbf{M}_{TM} \leftarrow$ `template-matching` $(Frame, Template)$;
$Max_{corr} \leftarrow$ `max`$(\mathbf{M}_{TM})$;
$\mathbf{C}_0 \leftarrow$ `extract-coordinates`$(\mathbf{M}_{TM}, Max_{corr})$;
$\mathbf{C}'_{3\times3} \leftarrow \mathbf{C}_0 + \mathbf{C}_{3\times3}$;
$D \leftarrow (1/K_{6\times6})\times$`distance`$(\mathbf{C}'_{3\times3}, \mathbf{C}_{6\times6})$;

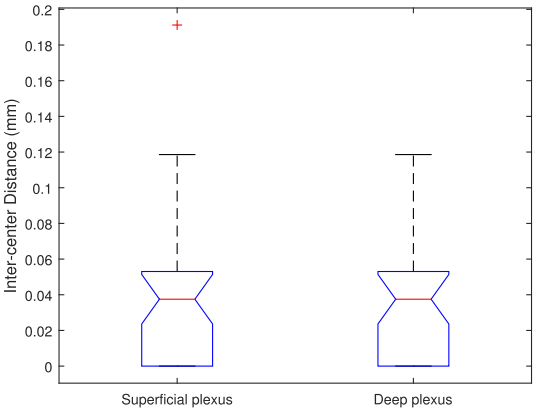

FIGURE 7. Box-plots of the inter-center distances considering each of the two FAZ centers obtained by the localization method when it is applied to the corresponding 6×6 mm^2 and 3×3 mm^2 "healthy" images in the first subset of the OCTAGON database (version 2).

when we assess the obtained location results based on their gold standard (100% success).

C. SEGMENTATION RESULTS

To evaluate the FAZ segmentation results, we use three well-known indexes in the related literature: Jaccard index [29], Dice score [30] and Hausdorff distance [31]. In particular, the Jaccard (J) index, and Dice (D) score is defined, respectively, as:

$$J = \frac{|A_{GS} \cap A_S|}{|A_{GS} \cup A_S|} \tag{5}$$

$$D = \frac{2\,|A_{GS} \cap A_S|}{|A_{GS}| + |A_S|} \tag{6}$$

where A_{GS} is the gold standard area, A_S, the segmented area, and $|x|$ represents the cardinality of x. Both indexes measure the degree of overlap between A_{GS} and A_S, being equal to 1 when the segmentation is perfect and equal to zero when there is no overlap. The Dice score is different from the Jaccard index which only counts true positives once in both the numerator and denominator. Additionally, the Hausdorff distance (HD) is defined as:

$$HD(A_{GS}, A_S) = \max\{d_1, d_2\} \tag{7}$$

being:

$$d_1 = \sup_{x\in A_{GS}} \inf_{y\in A_S} d(x, y)$$

$$d_2 = \sup_{y\in A_S} \inf_{x\in A_{GS}} d(x, y)$$

and where sup is the *supremum*, inf is the *infimum*, and $d(x, y)$ is the Euclidean distance. These three indexes are frequently used in the evaluation of numerous medical image segmentation methods [32], [33].

Tables 6 and 7 show the segmentation method results obtained for the "healthy" and "diabetic" images in the first subset of the OCTAGON database (version 2), respectively. In each table, the results are divided according to several scenarios (combinations for different values of zoom level, plexus depth and expert). With regards to the Jaccard index and Dice score, we can see that the method described in [20] is better than ours in the configuration "3×3 mm^2 plus superficial plexus" (regardless of the expert or if the image is "healthy" or "diabetic"). Conversely, our method performs better in the configuration "6×6 mm^2 plus deep plexus" (regardless of the expert or if the image is "healthy" or "diabetic"). In the rest of the configurations, the result of the comparison depends on the expert considered or the type of image ("healthy" or "diabetic"). Regarding the Hausdorff distance, in general, our approach gives better results. This could be interpreted as that the segmentation obtained by our approach adjusts better the expert's contour. Additionally, Table 8 shows the average Dice score obtained for each of the configuration criteria in isolation. From a global point of view (see the last column in this table), we can say that the behavior of both methods is very similar, although we can observe that our proposal is slightly better and presents somewhat less variability (lower standard deviation). Low variability is highly desired in the performance of any computational approach applied to medical image analysis. In any case, when interpreting these results, the high inter-observer variability of the two experts in each "healthy" image category must be taken into account (see Table 6). This makes it difficult to evaluate and compare the quality of the obtained

TABLE 6. Jaccard (J) index, Dice (D) score and Hausdorff Distance (HD) calculated for the "healthy" image FAZ segmentation in the first subset of the OCTAGON database (version 2). The standard deviation (SD) is also included. The best result in the comparison for each configuration and method is highlighted in bold.

Level of zoom	Method	Superficial			Deep		
		J±SD	D±SD	HD±SD (mm)	J±SD	D±SD	HD±SD (mm)
3×3 mm^2	Exp#1 *vs.* Exp#2	0.83 ± 0.04	0.91 ± 0.03	0.09 ± 0.04	0.72 ± 0.13	0.80 ± 0.11	0.16 ± 0.06
	Method [20] *vs.* Exp#1	$\mathbf{0.81 \pm 0.04}$	$\mathbf{0.90 \pm 0.03}$	0.13 ± 0.13	$\mathbf{0.74 \pm 0.11}$	$\mathbf{0.84 \pm 0.09}$	$\mathbf{0.15 \pm 0.13}$
	Proposed method *vs.* Exp#1	0.76 ± 0.06	0.87 ± 0.04	$\mathbf{0.12 \pm 0.04}$	0.69 ± 0.11	0.81 ± 0.08	0.16 ± 0.06
	Method [20] vs. Exp#2	$\mathbf{0.82 \pm 0.15}$	$\mathbf{0.90 \pm 0.04}$	0.11 ± 0.05	0.72 ± 0.11	0.82 ± 0.08	0.14 ± 0.05
	Proposed method *vs.* Exp#2	0.77 ± 0.07	0.87 ± 0.05	$\mathbf{0.11 \pm 0.04}$	$\mathbf{0.76 \pm 0.10}$	$\mathbf{0.86 \pm 0.07}$	$\mathbf{0.13 \pm 0.05}$
6×6 mm^2	Exp#1 *vs.* Exp#2	0.72 ± 0.10	0.82 ± 0.07	0.13 ± 0.05	0.68 ± 0.09	0.80 ± 0.07	0.16 ± 0.05
	Method [20] *vs.* Exp#1	0.72 ± 0.16	0.79 ± 0.16	0.31 ± 0.75	0.66 ± 0.09	0.79 ± 0.07	0.18 ± 0.06
	Proposed method *vs.* Exp#1	$\mathbf{0.73 \pm 0.08}$	$\mathbf{0.84 \pm 0.06}$	$\mathbf{0.13 \pm 0.05}$	$\mathbf{0.68 \pm 0.10}$	$\mathbf{0.81 \pm 0.07}$	$\mathbf{0.17 \pm 0.07}$
	Method [20] *vs.* Exp#2	$\mathbf{0.77 \pm 0.19}$	0.81 ± 0.19	0.14 ± 0.14	0.72 ± 0.09	0.83 ± 0.06	0.15 ± 0.06
	Proposed method *vs.* Exp#2	0.75 ± 0.08	$\mathbf{0.86 \pm 0.06}$	$\mathbf{0.12 \pm 0.05}$	$\mathbf{0.76 \pm 0.08}$	$\mathbf{0.86 \pm 0.05}$	$\mathbf{0.14 \pm 0.07}$

TABLE 7. Jaccard (J) index, Dice (D) score and Hausdorff Distance (HD) calculated for the "diabetic" image FAZ segmentation in the first subset of the OCTAGON database (version 2). The standard deviation (SD) is also included. The best result in the comparison for each configuration is highlighted in bold.

Level of zoom	Method	Superficial			Deep		
		J±SD	D±SD	HD±SD (mm)	J±SD	D±SD	HD±SD (mm)
3×3 mm^2	Method [20]	$\mathbf{0.83 \pm 0.06}$	$\mathbf{0.90 \pm 0.04}$	$\mathbf{0.08 \pm 0.04}$	0.69 ± 0.10	0.81 ± 0.08	$\mathbf{0.16 \pm 0.06}$
	Proposed method	0.76 ± 0.08	0.86 ± 0.06	0.14 ± 0.07	$\mathbf{0.71 \pm 0.13}$	$\mathbf{0.82 \pm 0.10}$	0.17 ± 0.11
6×6 mm^2	Method [20]	$\mathbf{0.75 \pm 0.08}$	$\mathbf{0.86 \pm 0.05}$	$\mathbf{0.14 \pm 0.07}$	0.64 ± 0.20	0.76 ± 0.21	0.27 ± 0.32
	Proposed method	0.73 ± 0.05	0.84 ± 0.04	0.15 ± 0.06	$\mathbf{0.72 \pm 0.13}$	$\mathbf{0.83 \pm 0.10}$	$\mathbf{0.20 \pm 0.16}$

TABLE 8. Comparison of the average Dice score obtained for the FAZ segmentation in the first subset of the OCTAGON database (version 2), considering each of the configuration criteria in isolation. The best result in the comparison for each criterion is highlighted in bold. The label "SD" denotes standard deviation. Note that the "diabetic" images were only labeled by one expert.

Method	3×3mm^2	6×6mm^2	Sup.	Deep	Healt.	Diab.	Total±SD
Method [20] *vs.* Exp#1	$\mathbf{0.86 \pm 0.04}$	0.80 ± 0.04	$\mathbf{0.86 \pm 0.05}$	0.80 ± 0.03	0.83 ± 0.05	0.83 ± 0.06	0.83 ± 0.03
Proposed method *vs.* Exp#1	0.84 ± 0.03	$\mathbf{0.83 \pm 0.01}$	0.85 ± 0.01	$\mathbf{0.82 \pm 0.01}$	$\mathbf{0.83 \pm 0.03}$	$\mathbf{0.84 \pm 0.02}$	$\mathbf{0.84 \pm 0.01}$
Method [20] *vs.* Exp#2	$\mathbf{0.86 \pm 0.05}$	0.81 ± 0.04	$\mathbf{0.87 \pm 0.04}$	0.80 ± 0.03	0.84 ± 0.04	–	0.84 ± 0.03
Proposed method *vs.* Exp#2	0.85 ± 0.02	$\mathbf{0.85 \pm 0.01}$	0.86 ± 0.01	$\mathbf{0.84 \pm 0.02}$	$\mathbf{0.86 \pm 0.01}$	–	$\mathbf{0.85 \pm 0.01}$

segmentation results since it is hard to select an appropriate gold standard based on which to perform a fair evaluation or comparison. Additionally, Figs. 8 and 9 allow us to compare the best and worst FAZ segmentation results for the "healthy" and "diabetic" images, respectively. In Fig. 8, the segmentation of expert#1 is used as a reference to order the segmentation results from best to worst regarding the value provided by the Dice score.

To study the behavior of our segmentation method in more noisy and pathological images, we show in Table 9 the results obtained in the second subset of the OCTAGON database (version 2). Although each image in this subset is included in one of the three categories shown in the mentioned table, some of them could simultaneously belong to several of these categories or, in other cases, belong to a new category related to a high degree of FAZ damage. All this makes the FAZ segmentation task in this subset harder than the first subset of images, as can be seen when the standard deviations are compared: much higher in the second subset than in the first. Figure 10 allows us to compare our best and worst segmentation results with the expert and also clearly shows the degree of difficulty associated with the images

TABLE 9. Jaccard (J) index, Dice (D) score and Hausdorff Distance (HD) calculated for the images in the second subset of the OCTAGON database (version 2). The label "SD" denotes standard deviation.

Category	J±SD	D±SD	HD±SD (mm)
With ischemia	0.58 ± 0.14	0.72 ± 0.12	0.40 ± 0.34
With artifacts	0.50 ± 0.25	0.63 ± 0.26	0.39 ± 0.38
Not centered in the FAZ	0.60 ± 0.11	0.74 ± 0.09	0.25 ± 0.16
All of images	0.56 ± 0.17	0.70 ± 0.17	0.35 ± 0.31

that belong to this subset. These results corroborate that the proposed segmentation method not only offers satisfactory results in normal and typical foveal conditions but also in those noisy and pathological scenarios that are common in clinical practice.

We can also compare our proposal with other works. However, the comparison will not be fair because the approach proposed here is fully automatic and those proposals existing in the related literature are semi-automatic. Furthermore, in some cases, the comparison of results may be impossible because other proposals focused on addressing the diagnostic task and not on evaluating the quality of the

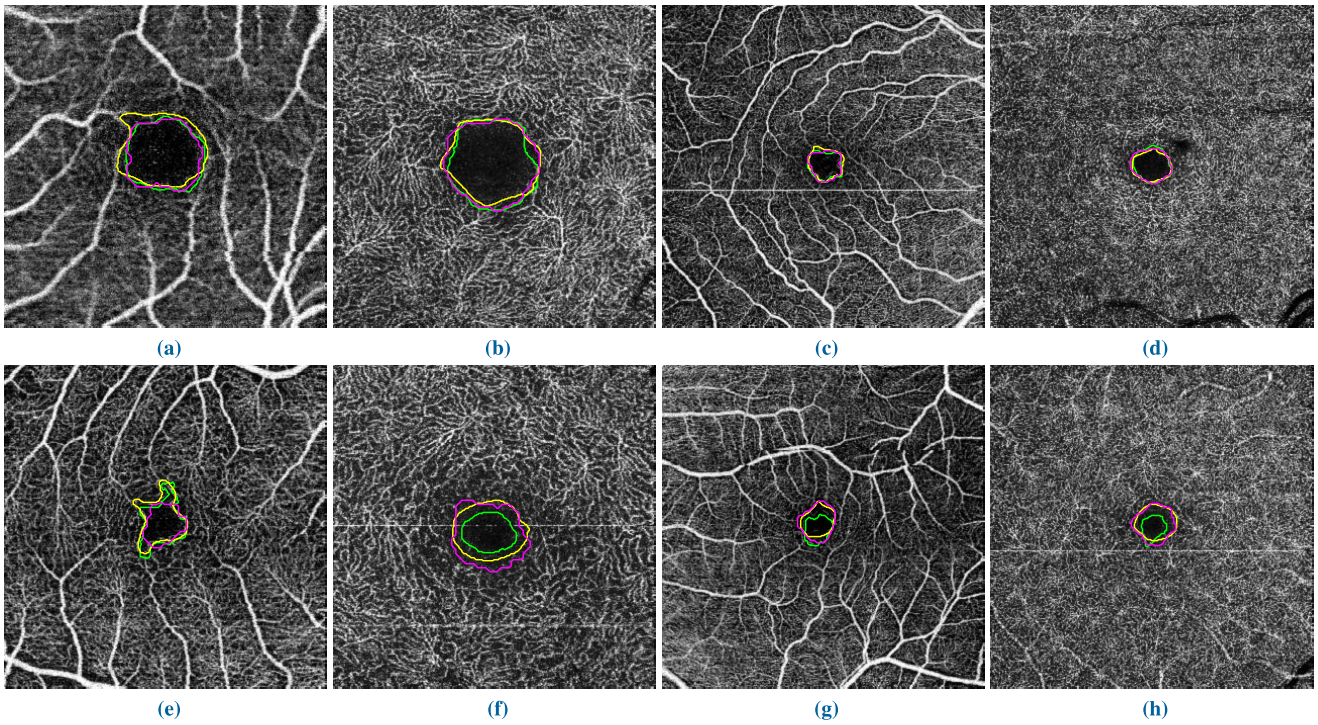

FIGURE 8. Comparing the best (1st row) and worst (2nd row) FAZ segmentation results (magenta) with expert#1 (green) for the "healthy" images in the first subset of the OCTAGON database (version 2). The expert#2's segmentation (yellow) is also shown: (a) 3×3 mm^2 superf. plexus ($D_1 = 0.94$, $D_2 = 0.86$); (b) 3×3 mm^2 deep plexus ($D_1 = 0.93$, $D_2 = 0.93$); (c) 6×6 mm^2 superf. plexus ($D_1 = 0.92$, $D_2 = 0.91$); (d) 6×6 mm^2 deep plexus ($D_1 = 0.94$, $D_2 = 0.93$); (e) 3×3 mm^2 superf. plexus ($D_1 = 0.77$, $D_2 = 0.73$); (f) 3×3 mm^2 deep plexus ($D_1 = 0.59$, $D_2 = 0.85$); (g) 6×6 mm^2 superf. plexus ($D_1 = 0.68$, $D_2 = 0.88$); (h) 6×6 mm^2 deep plexus ($D_1 = 0.58$, $D_2 = 0.89$). The variable D_i denotes the Dice score regarding the expert#i.

obtained segmentation. For example, in the Alam *et al.*'s approach [18], there were two steps with human intervention: the contour of the FAZ was semi-automatically delimited and the center of the fovea was placed manually. The reason for manually providing this kind of information is that their main goal was to obtain the FAZ area as accurately as possible. In particular, a comparison of the FAZ area for normal patients and patients with sickle cell disease was reported. Similarly, in [19], the FAZ segmentation process also required human intervention (the fovea center was manually selected) and the goal of this study was to make an early diagnosis of DR. Therefore, different performance measures from different classifiers, which distinguish sub-clinical RD patients from normal cases, were provided. Finally, in the Lu *et al.*'s approach [17], manual selection of the fovea center was also required. However, in this case, for the configuration "$3 \times 3\,\text{mm}^2$ plus superficial layer", we can compare their Jaccard index results, 0.87 and 0.86 in healthy and diabetic cases, respectively, with our proposal, 0.77 and 0.76, respectively. However, to add context to this comparison, it should be noted that the scope of our proposal is wider (it includes more configuration criteria, such as $6 \times 6\,\text{mm}^2$ zoom level and deep plexus) and the images of the dataset used are better adjusted to the real conditions faced by the expert clinicians, including significant variability in the different scenarios analyzed. For example, our first subset of images contains 69 diabetic OCT-A images with advanced stages of RD, whereas the dataset of [17] contains 66 images, being 16 of them without RD, 22 mild to moderate RD and 28 with severe RD. Furthermore, our approach also provides acceptable results under more difficult conditions, as is the case of the second subset of the OCTAGON database, which is characterized by images with the presence of ischemia or artifacts, or by images not centered in the FAZ.

Finally, we analyze the computational cost associated with the methods implemented in this work. Thus, the average costs of the localization method (including its standard deviation) were 133.2 ± 15.9 and 234.8 ± 30.9 ms/image for the 3×3 mm^2 and 6×6 mm^2 level of zoom, respectively. On the other hand, the average costs of the segmentation method, including the cost associated with the FAZ center search, were 148.4 ± 16.0 and 262.6 ± 25.3 ms/image for the $3 \times 3\,\text{mm}^2$ and $6 \times 6\,\text{mm}^2$ level of zoom, respectively. These costs were obtained for a code implemented in MATLAB and using a computer with a processor Intel Core i5-3350CPU @ 3.10GHz (8GB RAM). Note that much of the computational cost associated with the segmentation process corresponds to the process of localizing the FAZ center. This is so since the convolution process associated with template matching has a much higher cost than that associated with the adaptive binarization process. In any case, the magnitude order of the times obtained for both methods is not prohibitive. The

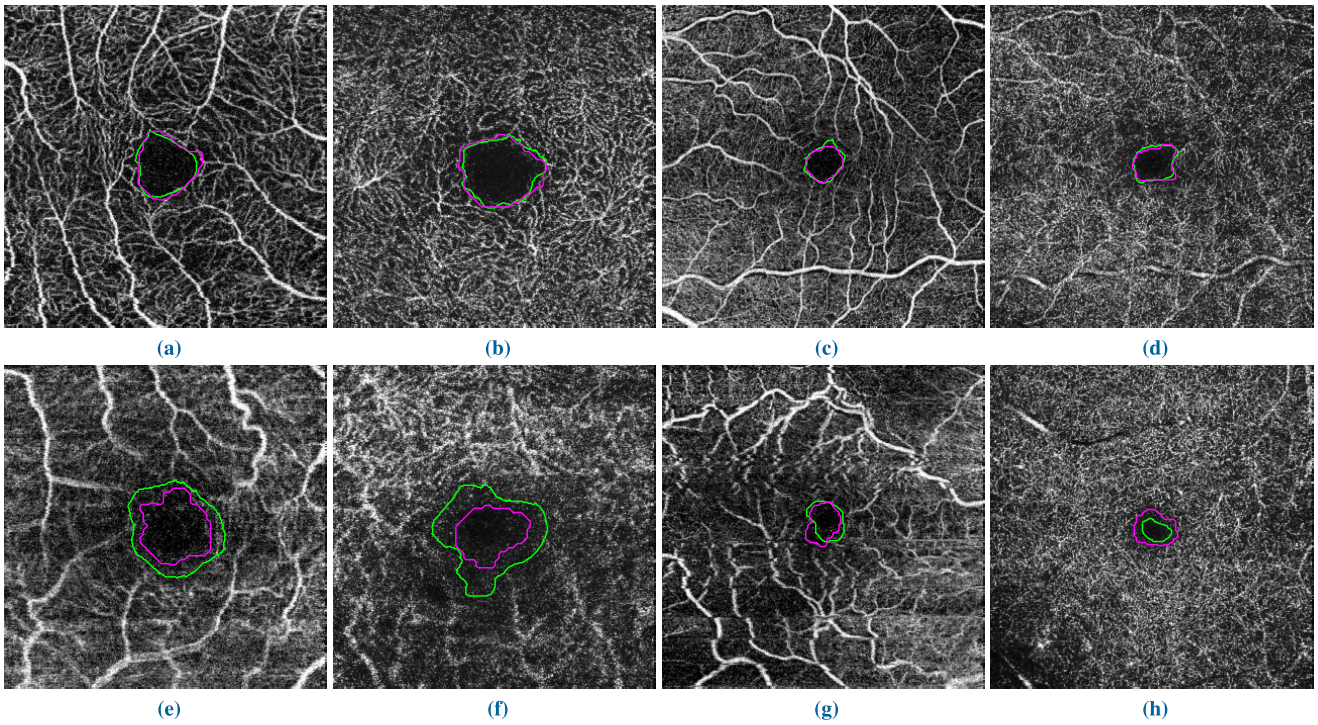

FIGURE 9. Comparing the best (1st row) and worst (2nd row) FAZ segmentation results (magenta) with expert's segmentation (green) for the "diabetic" images in the first subset of the OCTAGON database (version 2): (a) 3×3 mm^2 superf. plexus ($D = 0.93$); (b) 3×3 mm^2 deep plexus ($D = 0.93$); (c)6×6 mm^2 superf. plexus ($D = 0.91$); (d) 6×6 mm^2 deep plexus ($D = 0.92$); (e) 3×3 mm^2 superf. plexus ($D = 0.73$); (f) 3×3 mm^2 deep plexus ($D = 0.58$); (g) 6×6 mm^2 superf. plexus ($D = 0.76$); (h) 6×6 mm^2 deep plexus ($D = 0.58$). The variable D denotes the Dice score.

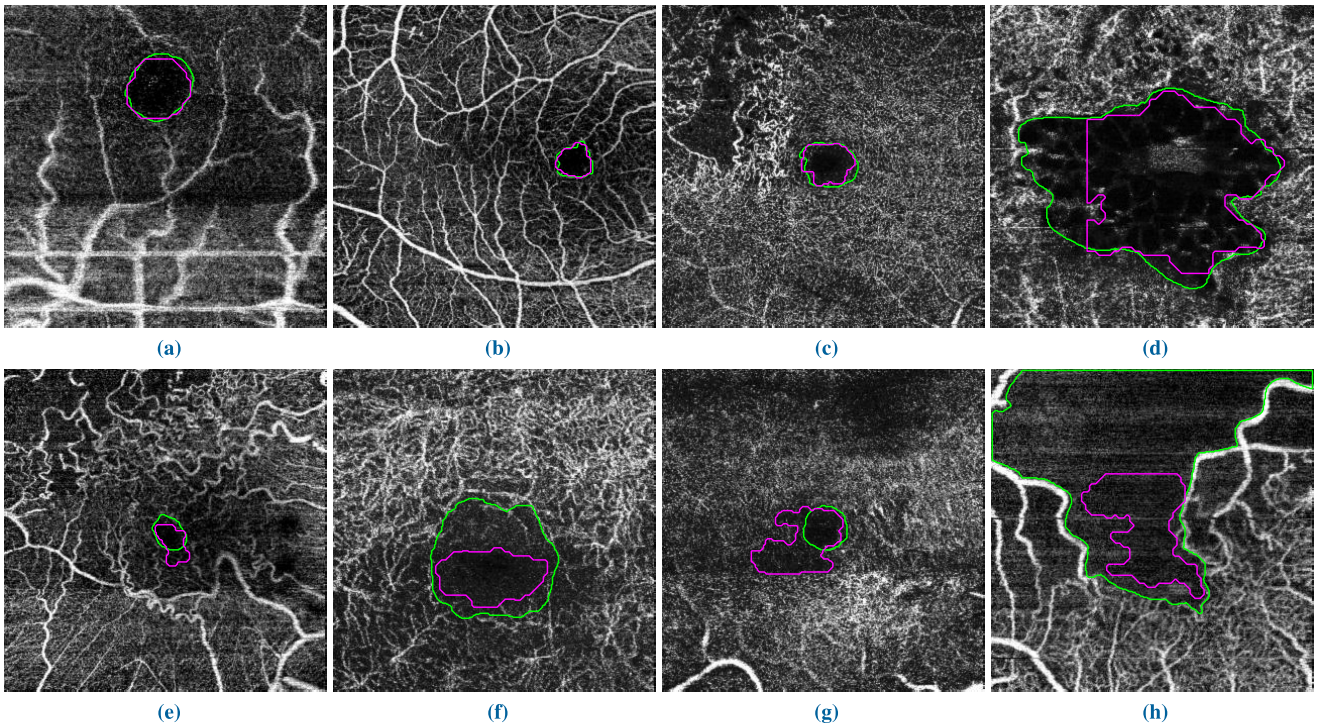

FIGURE 10. Comparing the best (1st row) and worst (2nd row) FAZ segmentation results (magenta) with expert's segmentation (green) for the images in the second subset of the OCTAGON database (version 2): (a) artifacts (and image not centered in the FAZ) ($D = 0.92$); (b) image not centered in the FAZ ($D = 0.91$); (c) ischemia ($D = 0.89$); (d) ischemia ($D = 0.83$); (e) ischemia ($D = 0.65$); (f) ischemia ($D = 0.57$); (g) artifacts ($D = 0.46$); (h) ischemia ($D = 0.35$). The variable D denotes the Dice score.

cost could be reduced even more if a compiled language is used instead of an interpreted language, as is the case of MATLAB.

V. CONCLUSION

This paper presents a new approach for modeling, localizing, and segmenting the FAZ in OCT-A images. The first stage

generates two FAZ normality models (superficial and deep plexus). The second stage uses the FAZ model created in the first stage to define a robust method based on template matching that allows us to automatically localize the FAZ center. Finally, the third stage uses the FAZ center obtained in the second stage to define a method based on an adaptive binarization process that segments the FAZ region. The localization and segmentation methods are validated in the OCTAGON database (version 2). This database is public and contains two image subsets with different scenarios (''diabetic''/''healthy'', superficial/deep plexus, and two levels of zoom) and different levels of complexity.

In terms of localization, we obtained a SR of 100% and 96% in the first and second subset of images, respectively. These results evidence that: (i) the two generated FAZ normality models (3×3 mm^2) are enough to address the localization problem, independently of the level of zoom, level of depth, and absence/presence of noise and pathology of the images considered; and (ii) the localization method exhibits a robust behavior, given that it also works quite well in images with serious limitations, including the presence of ischemia, artifacts, or images not centered in the FAZ. Additionally, we propose a simple mechanism based on template matching to compare the FAZ centers obtained in two OCT-A images of the same patient's eye, but with different level of zoom (3×3 mm^2 and 6×6 mm^2). This mechanism represents a new procedure to automatically validate any FAZ localization method in OCT-A images. In particular, when it is applied to evaluate our method, the obtained results support the hypothesis of being a robust localization method.

Finally, the segmentation results obtained in the first subset of images were significantly stable and competitive. Thus, the global average values of the Dice score (including its standard deviation) were 0.84 ± 0.01 and 0.85 ± 0.01, when compared to the expert 1 and 2, respectively. The low standard deviation obtained explains the fairly homogeneous behavior of the method in the different configurations of this dataset. The global average value of the Dice score in the second subset of images was 0.70 ± 0.17. However, it is important to note that the last subset contains images in which FAZ segmentation is a more difficult task to accomplish than in the first subset.

DECLARATION OF INTERESTS

The authors declare that they have no known competing financial interests or personal relationships that could have appeared to influence the work reported in this paper.

REFERENCES

[1] T. E. de Carlo, A. Romano, N. K. Waheed, and J. S. Duker, ''A review of optical coherence tomography angiography (OCTA),'' *Int. J. Retina Vitreous*, vol. 1, no. 1, p. 5, Apr. 2015.

[2] H. A. Nugroho, D. A. Dharmawan, N. A. Litasari, and L. Listyalina, ''Automated segmentation of foveal avascular zone in digital colour retinal fundus images,'' *Int. J. Biomed. Eng. Technol.*, vol. 23, no. 1, p. 1, 2017.

[3] C. Balaratnasingam, M. Inoue, S. Ahn, J. McCann, E. Dhrami-Gavazi, L. A. Yannuzzi, and K. B. Freund, ''Visual acuity is correlated with the area of the foveal avascular zone in diabetic retinopathy and retinal vein occlusion,'' *Ophthalmology*, vol. 123, no. 11, pp. 2352–2367, Nov. 2016.

[4] M. C. Salles, A. Kvanta, U. Amrén, and D. Epstein, ''Optical coherence tomography angiography in central retinal vein occlusion: Correlation between the foveal avascular zone and visual acuity,'' *Investigative Opthalmol. Vis. Sci.*, vol. 57, no. 9, pp. OCT242–OCT246, Jul. 2016.

[5] J.-W. Kang, R. Yoo, Y. H. Jo, and H. C. Kim, ''Correlation of microvascular structures on optical coherence tomography angiography with visual acuity in retinal vein occlusion,'' *Retina*, vol. 37, no. 9, pp. 1700–1709, 2017.

[6] Y.-C. Chen, Y.-T. Chen, and S.-N. Chen, ''Foveal microvascular anomalies on optical coherence tomography angiography and the correlation with foveal thickness and visual acuity in retinopathy of prematurity,'' *Graefe's Arch. Clin. Experim. Ophthalmol.*, vol. 257, no. 1, pp. 23–30, 2019.

[7] A. Demircan, C. Yesilkaya, C. Altan, Z. Alkin, D. Yasa, E. D. Aygit, and D. Bektasoglu, ''Foveal avascular zone area measurements with optical coherence tomography angiography in patients with nanophthalmos,'' *Eye*, vol. 33, no. 3, pp. 445–450, Mar. 2019.

[8] J. Kwon, J. Choi, J. W. Shin, J. Lee, and M. S. Kook, ''Alterations of the foveal avascular zone measured by optical coherence tomography angiography in glaucoma patients with central visual field defects,'' *Investigative Ophthalmol. Vis. Sci.*, vol. 58, no. 3, pp. 1637–1645, 2017.

[9] M. Fadzil, L. Izhar, and H. Nugroho, ''Analysis of foveal avascular zone for grading of diabetic retinopathy,'' *Int. J. Biomed. Eng. Technol.*, vol. 6, no. 3, pp. 232–250, 2011.

[10] E. Çiloğlu, F. Unal, E. A. Sukgen, Y. Kocluk, and N. C. Dogan, ''Evaluation of foveal avascular zone and capillary plexus in smokers using optical coherence tomography angiography,'' *J. Current Ophthalmol.*, to be published. [Online]. Available: https://www.sciencedirect.com/science/article/pii/S2452232519301738, doi: 10.1016/j.joco.2019.09.002.

[11] B. D. Krawitz, S. Mo, L. S. Geyman, S. A. Agemy, N. K. Scripsema, P. M. Garcia, T. Y. P. Chui, and R. B. Rosen, ''Acircularity index and axis ratio of the foveal avascular zone in diabetic eyes and healthy controls measured by optical coherence tomography angiography,'' *Vis. Res.*, vol. 139, pp. 177–186, Oct. 2017.

[12] A. G. Silva, M. S. Fouto, A. T. da Silva, R. Arthur, A. M. Arthur, Y. Iano, and J. M. L. de Faria, ''Segmentation of foveal avascular zone of the retina based on morphological alternating sequential filtering,'' in *Proc. IEEE 28th Int. Symp. Comput.-Based Med. Syst.*, Jun. 2015, pp. 38–43.

[13] H. A. Nugroho, D. Purnamasari, I. Soesanti, W. K. Oktoeberza, and D. A. Dharmawan, ''Segmentation of foveal avascular zone in colour fundus images based on retinal capillary endpoints detection,'' *J. Telecommun., Electron. Comput. Eng.*, vol. 9, nos. 3–8, pp. 107–112, 2017.

[14] A. F. M. Hani, N. F. Ngah, T. M. George, L. I. Izhar, H. Nugroho, and H. A. Nugroho, ''Analysis of foveal avascular zone in colour fundus images for grading of diabetic retinopathy severity,'' in *Proc. Annu. Int. Conf. IEEE Eng. Med. Biol.*, Aug. 2010, pp. 5632–5635.

[15] S. Hajeb Mohammad Alipour, H. Rabbani, and M. Akhlaghi, ''A new combined method based on curvelet transform and morphological operators for automatic detection of foveal avascular zone,'' *Signal, Image Video Process.*, vol. 8, no. 2, pp. 205–222, Feb. 2014.

[16] D. Hofer, J. I. Orlando, P. Seeböck, G. Mylonas, F. Goldbach, A. Sadeghipour, B. S. Gerendas, and U. Schmidt-Erfurth, ''Foveal avascular zone segmentation in clinical routine fluorescein angiographies using multitask learning,'' in *Proc. Int. Workshop Ophthalmic Med. Image Anal.* Cham, Switzerland: Springer, 2019, pp. 35–42.

[17] Y. Lu, J. M. Simonett, J. Wang, M. Zhang, T. Hwang, A. M. Hagag, D. Huang, D. Li, and Y. Jia, ''Evaluation of automatically quantified foveal avascular zone metrics for diagnosis of diabetic retinopathy using optical coherence tomography angiography,'' *Investigative Ophthalmol. Vis. Sci.*, vol. 59, no. 6, pp. 2212–2221, 2018.

[18] M. Alam, D. Thapa, J. I. Lim, D. Cao, and X. Yao, ''Quantitative characteristics of sickle cell retinopathy in optical coherence tomography angiography,'' *Biomed. Opt. Express*, vol. 8, no. 3, pp. 1741–1753, 2017.

[19] N. Eladawi, M. Elmogy, L. Fraiwan, F. Pichi, M. Ghazal, A. Aboelfetouh, A. Riad, R. Keynton, S. Schaal, and A. El-Baz, ''Early diagnosis of diabetic retinopathy in OCTA images based on local analysis of retinal blood vessels and foveal avascular zone,'' in *Proc. 24th Int. Conf. Pattern Recognit. (ICPR)*, Aug. 2018, pp. 3886–3891.

[20] M. Díaz, J. Novo, P. Cutrín, F. Gómez-Ulla, M. G. Penedo, and M. Ortega, ''Automatic segmentation of the foveal avascular zone in ophthalmological OCT—A images,'' *PLoS ONE*, vol. 14, no. 2, pp. 1–22, 2019.

[21] OCTAGON. (2018). *Angiography By Optical Coherence Tomography (OCT-A) Images Used to the Segmentation of the Foveal Avascular Zone*. Accessed: Jun. 1, 2020. [Online]. Available: http://www.varpa.es/research/ophtalmology.html
[22] N. Iafe, N. Phasukkijwatana, X. Chen, and D. Sarraf, "Retinal capillary density and foveal avascular zone area are age-dependent: Quantitative analysis using optical coherence tomography angiography," *Investigative Opthalmol. Vis. Sci.*, vol. 57, pp. 5780–5787, 2016.
[23] F. Ghassemi, R. Mirshahi, F. Bazvand, K. Fadakar, H. Faghihi, and S. Sabour, "The quantitative measurements of foveal avascular zone using optical coherence tomography angiography in normal volunteers," *J. Current Ophthalmol.*, vol. 29, no. 4, pp. 293–299, Dec. 2017.
[24] A. Rosenfeld, "Picture processing by computer," *ACM Comput. Surv.*, vol. 1, no. 3, pp. 147–176, 1969.
[25] R. Brunelli, *Template Matching Techniques in Computer Vision: Theory and Practice*. Hoboken, NJ, USA: Wiley, 2009.
[26] S. Sun, H. Park, D. R. Haynor, and Y. Kim, "Fast template matching using correlation-based adaptive predictive search," *Int. J. Imag. Syst. Technol.*, vol. 13, no. 3, pp. 169–178, 2003.
[27] J. Sauvola and M. Pietikäinen, "Adaptive document image binarization," *Pattern Recognit.*, vol. 33, no. 2, pp. 225–236, Feb. 2000.
[28] N. Chaki, S. H. Shaikh, and K. Saeed, *A Comprehensive Survey on Image Binarization Techniques*. New Delhi, India: Springer, 2014, pp. 5–15.
[29] R. Real and J. M. Vargas, "The probabilistic basis of Jaccard's index of similarity," *Systematic Biol.*, vol. 45, no. 3, pp. 380–385, Sep. 1996.
[30] L. R. Dice, "Measures of the amount of ecologic association between species," *Ecology*, vol. 26, no. 3, pp. 297–302, Jul. 1945.
[31] N. Aspert, D. Santa-Cruz, and T. Ebrahimi, "MESH: Measuring errors between surfaces using the hausdorff distance," in *Proc. IEEE Int. Conf. Multimedia Expo*, vol. 1, Aug. 2002, pp. 705–708.
[32] V. Chalana and Y. Kim, "A methodology for evaluation of boundary detection algorithms on medical images," *IEEE Trans. Med. Imag.*, vol. 16, no. 5, pp. 642–652, Oct. 1997.
[33] J. Bertels, T. Eelbode, M. Berman, D. Vandermeulen, F. Maes, R. Bisschops, and M. B. Blaschko, "Optimizing the Dice score and Jaccard index for medical image segmentation: Theory and practice," in *Medical Image Computing and Computer Assisted Intervention—MICCAI*, D. Shen, Eds. Cham, Switzerland: Springer, 2019, pp. 92–100.

ENRIQUE J. CARMONA received the M.S. degree in electronic engineering from the University of Granada, Spain, in 1996, and the Ph.D. degree in physics from the Universidad Nacional de Educación a Distancia (UNED), Madrid, Spain, in 2003. Since 2009, he has been an Associate Professor with the Department of Artificial Intelligence, School of Computer Engineering, UNED. His research interests include computer vision, evolutionary computation, and the application of the latter to different areas (medical images, aeronautics, electronics, and mathematics).

MACARENA DÍAZ received the degree in computer engineering and the M.Sc. degree in bioinformatics from the University of A Coruña, Spain, in 2017 and 2019, respectively. She is currently pursuing the Ph.D. degree in computer science in a collaborative project between the ophthalmology and computing centers in Galicia, Madrid, and the University of A Coruña. Her main research interests include computer vision and biomedical imaging processing.

JORGE NOVO received the M.Sc. and Ph.D. degrees *(cum laude)* in computer science from the University of A Coruña, in 2007 and 2012, respectively. He was a Visiting Researcher involved in CMR images in the detection of landmark points at Imperial College London and a Postdoctoral Research Fellow at the INEB and INESC-TEC research institutes in the development of CAD systems for lung cancer diagnosis with chest CT images. His main research interests include computer vision, pattern recognition, and biomedical image processing.

MARCOS ORTEGA received the degree in computer science, in 2004, and the Ph.D. degree in computer science, in 2009. He currently serves as an Associate Professor at the University of A Coruña, where he is teaching mainly in the Faculty of Computer Science and is also serving as the Secretary. He is also Researcher at the Research Centre in Information and Communication Technologies (CITIC), a member of its scientific committee, and its Representative in the ECHAlliance. He is also a member of the Institute of Biomedical Research of A Coruña (INIBIC) with a rank of Principal Investigator. His research interests include computer vision, medical image processing, and medical informatics.